

****TITLE****

*ASP Conference Series, Vol. **VOLUME**, **YEAR OF PUBLICATION***
****NAMES OF EDITORS****

Numerical Study of Rotating Convection

Kwing L. Chan

Department of Mathematics, The Hong Kong University of Science and Technology, Clear Water Bay, Hong Kong, China

Abstract. New results and numerical issues relevant to stellar convection in rotating stars are discussed.

1. Introduction

All stars are rotating, but the hydrodynamics of rotating stars are poorly understood. A prominent example is the differential rotation in the convection zone of the sun, for which the rotation profile has been rather precisely determined from helioseismology (e.g. Thompson et al. 1996). The solar angular velocity distribution in the radial region $0.5r_{\odot} < r < r_{\odot}$ is characterized by two shear layers. One connects the rigidly rotating interior to the radially uniform but latitudinally differential rotation in the convection zone; the equator being faster than the higher latitudes. Another describes a drop of angular velocity from the deeper convective region to the outer boundary. Numerical simulations so far cannot produce a satisfactory explanation of the solar differential rotation.

An "explanation" should not simply be a numerical reproduction of the rotation profile. It has to be based on a framework of understanding of the interaction of convection and rotation, in parameter regimes relevant to stellar situations, so that inferences can be made for other stars. Numerical study of the general properties of rotating convection serves to build up this framework.

This paper contains three parts. The first part is an abridged review of previous studies of differential rotation. The second part presents new results based on f-box numerical experiments. The analysis will throw some light on the the parametric dependence of Reynolds stress and the generation of super-rotation at the equator. The third part addresses some numerical issues, some of which have been overlooked from time to time.

2. Previous Studies

Any theory of differential rotation must first be able to produce the solar differential rotation. Models trying to explain the solar differential rotation have been proposed since the early part of last century. In the beginning, since computing technology was not as highly developed as nowadays, essentially all of the theories were semi-analytical. 'Semi-analytical' means that they were not multidimensional computations solving the fluid equations directly; most of them still needed to use computers to solve some reduced sets of equations.

Table 1. A timeline of semi-analytical studies

	Reynolds stress models	latitude-dependent transport models
1932	Biermann	
1946	Wasiutynski	
1963	Kippenhahn	
1965		Weiss
1970	Kohler	
1971		Durney & Roxburgh
1977		Belvedere & Paterno
1979	Durney & Spruit	-----
1980	Rudiger	
1982	Schmidt	-----
1986	Pidatella et al.	-----
1987	Stix	-----
1989	Tuominen & Rudiger	-----
1992	Brandenburg et al.	-----
1993	Kitchatinov & Rudiger	
1993	Kuker et al.	
1994	Canuto et al.	
1999	Durney	-----
2001	Kuker & Stix	

Two broad categories of models based on two mechanisms have been proposed. The first category works through the momentum equation. It argues that under the influence of rotation, the convective turbulence becomes horizontally anisotropic and produce a Reynolds stress that can drive a differential rotation. The second category works through the energy equation. Since the angle between the rotation vector and the local gravity vector is a function of latitude, the inhibitive effect of rotation on convection would vary with latitude, and so would the efficiency of convective transport. This could induce a latitudinal entropy gradient which then sets up a differential rotation like a thermal wind in Earth’s atmosphere. Table 1 shows a timeline of illustrative examples in the two categories of models. Some studies included both mechanisms and they are labeled by the dashed lines in the ‘transport’ column. Recent versions of the Reynolds stress model (Kitchatinov & Rudiger 1992, Kuker et al. 1993) have been quite successful in reproducing the solar angular velocity distribution.

The semi-analytical models contain fitting parameters whose physical basis has to be verified. Some authors thus work on the fluid equations directly though numerical simulation (see Table 2). This approach was pioneered by Gilman in the nineteen seventies. His calculation used the Boussinesq approximation and was in a global shell geometry. His student, Glatzmaier, later extended the calculation by adopting the anelastic approximation and thus was able to handle the density stratification. Versions of Glatzmaier’s pseudo spectral anelastic code is still being used today (e.g. DeRosa, Gilman, & Toomre, 2002). The most recent shell model for the sun (Brun & Toomre 2002) used a rather high

Table 2. A timeline of numerical studies

	authors	geometry	size	grids per unit length
1977	Gilman	shell	$35 \times 30(\text{modes}) \times 9$	
1979	Gilman & Foukal	shell	$70 \times 20(\text{modes}) \times 8$	
1983	Hathaway & Sommerville	f-box	$32 \times 48 \times 25$	$7 \times 8 \times 25$
1984	Glatzmaier	shell	$T(32) \times 16(\text{modes})$	
1988	Hathaway & Sommerville	f-box	$48 \times 48 \times 25$	$10 \times 10 \times 25$
1993	Pulkkinen et al.	f-box	$31 \times 31 \times 31$	$16 \times 16 \times 31$
1994	Rieutord et al.	shell	$T(20) \times 32(\text{modes})$	
1995	Sun & Schubert	shell	$432 \times 216 \times 49$	
1996	Brandenburg et al.	f-box	$126 \times 126 \times 105$	$63 \times 63 \times 64$
1996	Brummell et al.	f-box	$96 \times 96 \times 64$	$24 \times 24 \times 64$
2000	Elliot	shell	$T(170) \times 33$	
2000	Miesh et al.	shell	$T(170) \times 98$	
2001	Chan	f-box	$35 \times 35 \times 39$	$23 \times 23 \times 39$
2001	Robinson & Chan	shell/box	$70 \times 70 \times 39$	$19 \times 19 \times 39$
2002	Brummell et al.	f-box	$128 \times 128 \times 192$	$21 \times 21 \times 96$
2002	Brun & Toomre	shell	$T(340) \times 193$	
current	Chan	f-box	$70 \times 70 \times 80$	$47 \times 47 \times 80$

spatial resolution. However, the total integration time was less than 18 years, far shorter than the thermal relaxation time of the solar convection zone ($> 10^5$ years). There are still substantial differences in the angular velocity distributions of the model and the observational data, particularly in the high latitude regions.

Another numerical approach is to study small pieces of the convection zone, so that the convective turbulence can be better resolved. The local region can be approximated as a rectangular box and the angle between the rotation vector and gravity can be treated as constant. Such a configuration is labeled as ‘f-box’ in Table 1 (*a la* ‘f-plane approximation’ used in Earth Science). Since the global flow cannot be included, its primary objective is to obtain information on the local turbulence. This approach was pioneered by the Boussinesq calculations of Hathaway & Sommerville in the nineteen eighties. Later calculations evolved towards compressibility and larger meshes.

I have been working with the ‘f-box’ approach since the early ninties (Chan & Mayr 1994). During that time, the computers were slower than those of today and the affordable meshes were generally smaller. To cover a sizable piece of parameter space with dense enough points, I needed to computed a rather large number of cases. Furthermore, thermal relaxation and statistical convergence both require long integration periods. The cases took a very long

Table 3. Turbulent velocity correlations and anisotropies of horizontal velocity/vorticity fluctuations of the old cases

$\frac{\theta}{\pi}$	Co	$\langle v'' \rangle$	$\langle \frac{v'_z v'_x}{v''_z v''_x} \rangle$	$\langle \frac{v'_z v'_y}{v''_z v''_y} \rangle$	$\langle \frac{v'_x v'_y}{v''_x v''_y} \rangle$	$\frac{\langle v''_y - v''_x \rangle}{\langle v'' \rangle}$	$\frac{\langle \zeta''_x - \zeta''_y \rangle}{\langle \zeta'' \rangle}$
0	0.80	0.16	0.00	0.00	0.00	0.00	0.00
1/8	0.79	0.16	0.02	-0.07	0.00	0.01	0.00
1/4	0.77	0.16	0.05	-0.09	-0.02	0.03	0.01
3/8	0.77	0.16	0.08	-0.09	-0.08	-0.01	0.00
7/16	0.77	0.16	0.07	-0.04	-0.06	-0.03	-0.01
1/2	0.78	0.16	0.00	-0.02	0.00	-0.01	-0.02
0	1.64	0.15	0.00	0.00	0.00	0.00	0.00
1/8	1.61	0.16	-0.02	-0.10	0.03	0.01	0.01
1/4	1.54	0.16	0.01	-0.13	0.06	0.03	0.02
3/8	1.49	0.17	0.04	-0.12	0.03	0.07	0.03
7/16	1.50	0.17	0.09	-0.12	-0.09	0.04	0.02
1/2	1.59	0.16	0.00	-0.03	0.00	-0.07	-0.07
0	3.46	0.14	0.00	0.00	0.00	0.00	0.00
1/8	3.24	0.15	-0.07	-0.10	0.02	0.00	0.01
1/4	3.09	0.16	-0.04	-0.14	0.08	0.01	0.04
3/8	2.85	0.18	0.04	-0.10	0.13	0.04	0.07
7/16	2.77	0.18	0.05	-0.07	0.14	0.11	0.08
1/2	3.20	0.16	0.00	-0.07	0.00	-0.18	-0.17
0	7.47	0.13	0.00	0.00	0.00	0.00	0.00
1/8	6.80	0.15	-0.12	-0.09	0.02	-0.01	0.02
1/4	6.23	0.16	-0.10	-0.11	0.06	0.01	0.06
3/8	5.77	0.17	0.03	-0.09	0.10	0.01	0.13
7/16	5.30	0.19	0.07	-0.03	0.17	0.06	0.16
1/2	7.58	0.13	0.00	-0.15	0.00	-0.15	-0.24

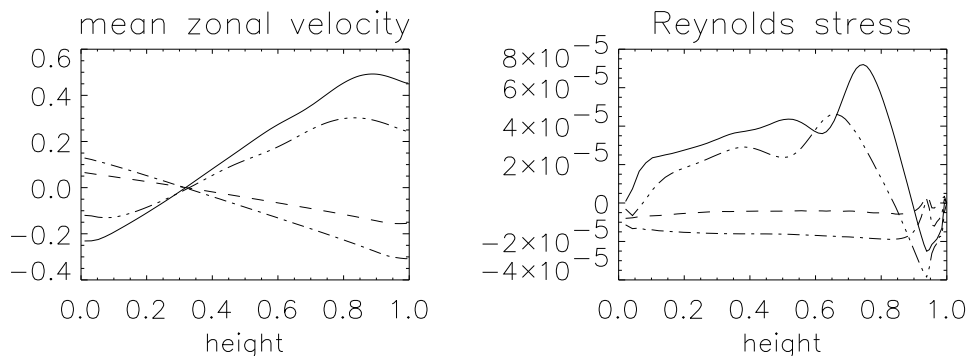
time to accumulate. The results were reported in a paper published in 2001. One interesting result is that the outer shear layer of the sun can be explained by the divergence of the vertical-meridional component of the Reynolds stress. Another is that the zonal-meridional component of the Reynolds stress undergoes a sign change as the Coriolis number varies. Here, I would like to elaborate on the discussion of this transition, as well as to describe some other highly relevant transitions.

3. Transitions in Reynolds Stress and Flow Structures

The specification of the numerical model is as following: (a) The compressible fluid equations are solve in a 3d f-box using finite-difference and explicit time stepping. (b) The angle between the rotation vector $\boldsymbol{\Omega}$ and $-\mathbf{x}$ (northward) corresponds to the colatitude (polar angle). The x, y, z axes represents the

Table 4. Turbulent velocity correlations and anisotropies of horizontal velocity/vorticity fluctuation of the new cases

$\frac{\theta}{\pi}$	Co	$\langle v'' \rangle$	$\langle \frac{v'_z v'_x}{v''_z v''_x} \rangle$	$\langle \frac{v'_z v'_y}{v''_z v''_y} \rangle$	$\langle \frac{v'_x v'_y}{v''_x v''_y} \rangle$	$\frac{\langle v''_y - v''_x \rangle}{\langle v'' \rangle}$	$\frac{\langle \zeta''_x - \zeta''_y \rangle}{\langle \zeta'' \rangle}$
1/2	1.52	0.08	0.00	0.00	-0.01	-0.06	-0.03
1/2	3.13	0.08	0.00	-0.01	0.00	-0.10	-0.09
1/2	4.78	0.10	0.00	0.01	0.00	0.26	0.06
1/2	7.90	0.09	0.00	0.02	0.00	0.21	0.04

Figure 1. Transition at the equator as Co goes through the values $3/2$ (dashed curves), 3 (dot-dashed curves), 6 (triple-dot-dashed curves), and 9 (solid curves). Left panel: horizontally and temporally averaged zonal velocity profiles. Right panel: vertical-zonal component of the Reynolds stress.

meridional (north to south), zonal (west to east), and the vertical directions, respectively. (c) The aspect ratio (width/height) is 1.5 (3 in a small number of cases). (d) The units are chosen such that the initial temperature, pressure, density at the top, and the total depth are 1 . (e) The layer $0 < z$ (height) < 0.95 is unstable; the layer $0.95 < z < 1$ is stable. (f) The upper and lower boundaries are impenetrable and stress-free; the side boundaries are periodic. (g) The temperature is fixed at the upper boundary; the input energy flux is fixed at the lower boundary ($= 0.03125$, or 0.00391).

The columns of Table 3 sequentially list: (1) the polar angle (scaled by π), (2) the Coriolis number (Co , based on the turbulence velocity), (3) the rms turbulence velocity, (4) the correlation of the vertical-meridional velocity fluctuations, (5) the correlation of the vertical-zonal velocity fluctuations, (6) the correlation of the zonal-meridional velocity fluctuations, (7) the horizontal turbulence velocity anisotropy (relative difference between the zonal and meridional rms velocity fluctuations), (8) the horizontal rms vorticity anisotropy (the relative difference between the meridional and zonal rms vorticity fluctuations). First, notice that the correlation of the two horizontal velocity components (Column 6) changes sign as the Coriolis number (Column 2) increases from below 1 to above 1 . It means that the zonal-meridional component of the Reynolds stress feeds momentum from higher to lower latitudes only when Co is high enough.

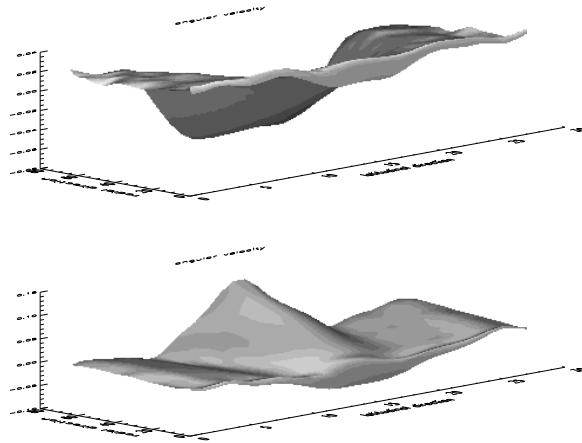


Figure 2. Angular velocity distributions in a shell computed by a spectral code using the ‘stratified approximation’ (Chan et al. 1994) for $Co \sim 3$ (upper panel) and ~ 12 (lower panel). A transition in the sense of the radial shear also occurs.

There is a qualitative change in the behavior of the fluid, this Reynolds stress component works for equatorial acceleration only for high Co values. The change is accompanied by a change of sign in the horizontal velocity anisotropy (Column 7) which in turn is accompanied by a change of sign in the vorticity anisotropy (Column 8, defined in an opposite sense of direction).

The close relationship between the horizontal velocity anisotropy and the vorticity anisotropy is not surprising. Vorticity anisotropy basically describes the preferred alignment of rolls along certain direction. The velocity accompanying such rolls would maximize along a perpendicular direction. Due to the action of the Coriolis force, the velocity anisotropy in turn would create an off-diagonal Reynolds stress component (cf. Rudiger 1989).

Higher resolution cases have recently been computed, that besides helping to check the older results, also allows for extending the parametric regime to higher Co numbers. Here I concentrate on discussing an interesting transition at the equator that occurs in the new parametric regime. The columns of Table 4 list the same kind of quantities as those of Table 3, but the colatitude is fixed at $\pi/2$. There is a transition between $Co \sim 3$ and $Co \sim 5$. The anisotropy of the horizontal velocity fluctuations and that of the horizontal vorticity fluctuations change sign between the two Co values. The correlation of the vertical-zonal velocity fluctuations also swithes sign, from negative to positive as Co increases; the zonal momentum transported by the Reynolds stress thus changes from downward to upward. The change in the direction of the zonal momentum transport induces a change in the sense of the shear in the mean zonal flow, as illustrated in Figure 1. The behavior of the higher Co flows is counter intuitive but highly relevant for understand the ‘superrotation’ at the equator of the solar convection zone. The transition in the f-box configuration also occurs in global shell calculations, between comparable Co values (see Figure 2).

The qualitative change in the properties of the convective turbulence is created by a change in the alignment of convective rolls (see Figure 3). At low

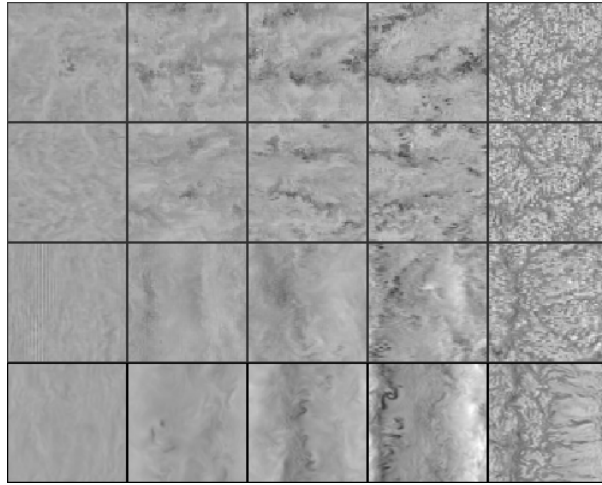


Figure 3. Each row shows horizontal cuts of an instantaneous vertical velocity field at different depths. The cases correspond to those of Figure 1. The value of Co increases towards the bottom. The structure of the flow changes from east-west aligning rolls to north-south aligning rolls.

Co values, the rolls align along the east-west direction. At higher Co values, the alignment turns to the north-south direction. Alignment parallel with the rotation vector can be readily understood by recalling the Taylor-Proudman theorem. Alignment perpendicular to the rotation vector might first seem puzzling. Actually, that is a direction of the mean shear flow. Alignment of convective rolls along the wind shear direction is a common phenomenon in the Earth's atmosphere, known as 'cloudstreets' (Lilly, 1966; Brown, 1979). It can also be understood in terms of preferential growth of linear modes (Hathaway, Gilman, & Toomre 1979). The negative shear (zonal mean velocity decreases upward) is just due to the conservation of angular momentum (Gilman & Foukal 1979). The positive shear is due to the two-dimensional nature of the flows (forced by the rotation); the cyclonic cells dominate over the anti-cyclonic cells.

What about the flow structures at higher latitudes? Figures 4 and 5, corresponding to Co values of approximately 6 and 9 respectively, provide examples of horizontal cuts of the vertical velocity field at different depths, for f-boxes at different latitudes. Roll structures are evident at mid/low latitudes (mainly north-south oriented). An interesting transition occurs at the pole where a 'polar vortex' develops at the higher Co value case.

4. Some Numerical Issues

Spatial resolution Figure 6 shows comparison of the mean zonal and meridional velocities calculated with different spatial resolutions, for the case $Co \sim 3$ and $\theta = 3\pi/8$. The agreements are very good, even for the original low resolution case.

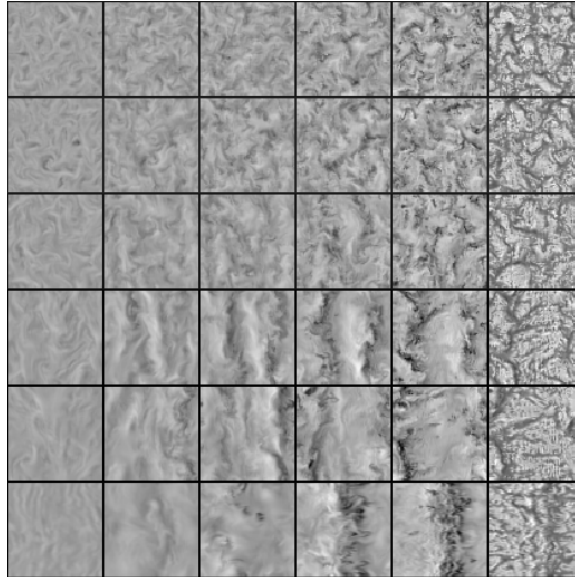


Figure 4. Horizontal cuts of vertical velocity fields at different depths for cases with $Co \sim 6$ at $\theta/\pi = 0, 1/8, 1/4, 3/8, 7/16,$ and $1/2$ (rows from top to bottom).

Thermal relaxation and statistical convergence Figure 7 compares the ‘time averaged’ profiles of the correlation coefficient of the vertical-zonal velocity fluctuations taken at different stages of evolution from initialization and for different lengths of temporal periods. It shows that both the thermal relaxation and the statistical convergence need long time (at least tens of percents of the Kelvin-Helmholtz time scale). One way to check for statistical convergence is to look at the zonal-meridional and vertical-zonal velocity correlations at the equator and the pole (also the vertical-meridional velocity correlation there). They should be 0 at all depths. Deviations of these quantities from 0 provide information on the accuracy of the averaging process. In the calculations described here, the typical errors of the correlations are about ± 0.01 (see the first row of Table 4).

Constant flux upper boundary condition Since the thermal relaxation time (τ_{th}) is very long, some authors tried to go around the problem by choosing a constant flux boundary condition at the top of the region, so that the output flux would always be the same as the input flux. Under such an arrangement, there can be no net exchange of energy between the box with outside. It would be interesting to check how good this could work.

Calculations were made to compare two cases, one with constant temperature and the other with constant flux at the top, all other parameters being the same. Figure 8 compares the two cases (left panels: constant temperature; right panels: constant flux). The top panels show evolution of the averaged flux profiles. In the initial stage (within a time period \leq a few percent of τ_{th} , the flux profiles of the constant flux case show some ‘convergence’ to uniformity. However, at later stages (time period \geq a few tens of percent of τ_{th}), large amplitude oscillations develop in the profile. On the other hand, the constant temperature

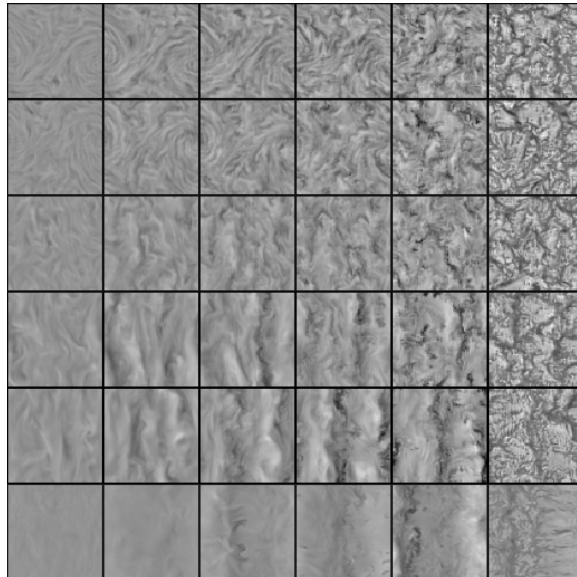


Figure 5. Similar to Figure 5, but $Co \sim 9$. A large vortex develops at the polar region.

case shows a steady convergence to a uniform profile. Comparison of the mean zonal velocity profiles is shown in the lower panels. Although the profiles appear to be quite similar in the later stage, they are very different in the early stage. The constant flux boundary condition cannot help to yield trustworthy velocity profiles when the integration time is not long enough.

5. Conclusions

(i) Geometry being simple, f-box calculations provides useful physical insights on the behavior of rotating convection relevant to the problem of differential rotation. (ii) Coherent roll-like structures either transversal or parallel to the rotation vector are closely related to the generation of the Reynolds stress. (iii) f-box rotating convection undergoes a number of transitions that change the qualitative nature of the various components of the Reynolds stress. A rather dense coverage of the parameter space is needed to sort out these changes. The Coriolis number is a key parameter that describes these transitions. (iv) Thermal relaxation and statistical convergence are both important. A sufficiently long integration in time is necessary for getting reliable results.

Acknowledgments. The author would like to thank the LOC/SOC of the 3D Star Workshop for the generous travel support. The research is supported by the Hong Kong Research Grants Council.

References

Belvedere, G., & Paterno, L. 1977, *Sol. Phys.*, 54, 289

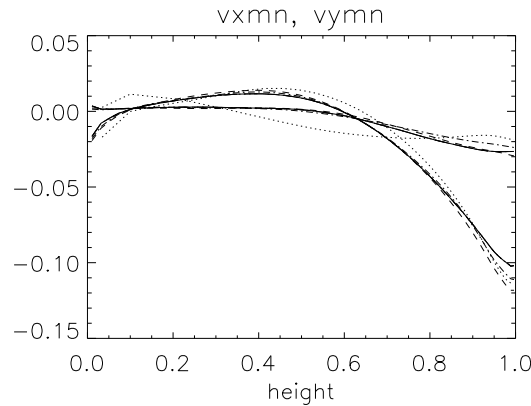


Figure 6. Mean zonal velocities (curves that show steep drops at the top) and mean meridional velocities computed with different mesh sizes and sub-grid-scale viscosity coefficients: $35 \times 35 \times 39$, $c_\mu = 2 \times (0.2)^2$ (dotted curve); $70 \times 70 \times 80$, $c_\mu = 2 \times (0.2)^2$ (dashed curve); $70 \times 70 \times 80$, $c_\mu = (0.2)^2$ (dot-dashed curve); $138 \times 138 \times 80$, $c_\mu = (0.2)^2$ (solid line). All for the same case with $Co \sim 3$ and $\theta/\pi = 3/8$.

- Biermann, L. 1932, *Z. Astrophys.*, 5, 117
 Brandenburg, A., Moss, D., & Tuominen, I. 1992, *A&A*, 465, 328
 Brandenburg, A., Jennings, R.L., Nordlund, A., Rieutord, M., Stein, R.F., & Tuominen, I. 1996, *J. Fluid Mech.*, 306, 325
 Brown, R.A. 1979, *J. Atmos. Sci.*, 27, 742
 Brummell, N.H., Hurlburt, N.E., & Toomre, J. 1996, *ApJ*, 473, 494
 Brummell, N.H., Clune, T.L., & Toomre, J. 2002, *ApJ*, 570, 825
 Brun, A.S. & Toomre, J. 2002, *ApJ*, 570, 865
 Canuto, V.M., Minotti, F.O., & Schilling, O. 1994, *ApJ*, 425, 303
 Chan, K.L. 2001, *ApJ*, 548, 1102
 Chan, K.L., Mayr, H.G. 1994, *Sol. Phys.*, 152, 283
 Chan, K.L., Mayr, H.G., Mengel, J.G., & Harris, I. 1994, *Sol. Phys.*, 152, 283
 DeRosa, M.L., Gilman, P.A., & Toomre, J. 2002, *ApJ*, in press
 Durney, B. 1999, *ApJ*, 511, 945
 Durney, B. & Roxburgh, I.W. 1971, *Sol. Phys.*, 16, 3
 Durney, B., & Spruit, H.C. 1979, *ApJ*, 234, 1067
 Elliot, J.R., Miesch, M.S., & Toomre, J. 2000, *ApJ*, 533, 546
 Gilman, P.A. 1977, *Geophys. Astrophys. Fluid Dyn.*, 8, 93
 Gilman, P.A., & Foukal, P.V. 1979, *ApJ*, 229, 1179
 Glatzmaier, G.A. 1984, *J. Comp. Phys.*, 55, 461
 Hatherway, D.H., Gilman, P.A., & Toomre, J. 1979, *Geophys. Astrophys. Fluid Dyn.*, 13, 289
 Hatherway, D.H., & Sommerville, R.C.J. 1983, *J. Fluid Mech.*, 126, 75

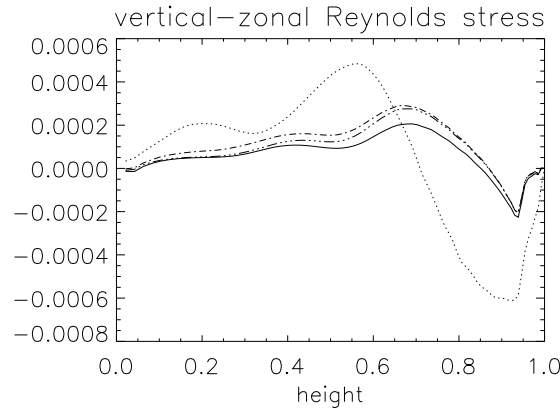


Figure 7. Profiles of the ‘averaged’ correlation coefficient of the vertical-zonal velocity fluctuations for the case at the equator with $Co \sim 6$. The averages are taken over different periods of time from start. The dotted, dot-dashed, triple-dot-dashed, and solid curves are for the periods $[98(\sim \tau_{th}/100), 126]$, $[1085(\sim \tau_{th}/10), 1195]$, $[1085, 1415]$, $[1085, 1745]$, respectively. When the period is within a few percent of the thermal relaxation time τ_{th} , the system is not relaxed. It takes at least ten percent of τ_{th} for the system to reach thermal relaxation. The convergence of the time averaging also needs about the same amount of integration time.

- Hatherway, D.H., & Sommerville, R.C.J. 1986, *J. Fluid Mech.*, 164, 91
 Kippenhahn, R. 1963, *ApJ*, 137, 664
 Kitchatinov, L.L., & Rudiger, G. 1993, *A&A*, 276, 96
 Kohler, H. 1970, *Sol. Phys.*, 13, 3
 Kuker, M., Rudiger, G. & Kitchatinov, L.L. 1993, *A&A*, 279, L1
 Kuker, M. & Stix, M. 2001, *A&A*, 366, 668
 Lilly, D.K. 1966, *J. Atmos. Sci.*, 23, 481
 Meish, M.S., Elliott, J.R., Toomre, J., Clune, T.L., Glatzmaier, G.A., & Gilman, P.A. 2000, *ApJ*, 532, 593
 Pidotella, R.M., Stix, M., Belvedere, G., & Paterno, L. 1986, *A&A*, 156, 22
 Pulkkinen, P., Tuominen, I., Brandenburg, A., Nordlund, A., & Stein, R.F. 1993, *A&A*, 267, 265
 Rieutord, M., Brandenburg, A., Mangeney, A., & Dorssart, P. 1994, *A&A*, 286, 471
 Robinson, F.J. & Chan, K.L. 2001, *MNRAS*, 321, 723
 Rudiger, G. 1980, *Geophys. Astrophys. Fluid Dyn.*, 16, 239
 Rudiger, G. 1989, *Differential Rotation and Stellar Convection: Sun and Solar Type Stars* (New York: Gordon and Breach)
 Schmidt, W. 1982, *Geophys. Astrophys. Fluid Dyn.*, 21, 27

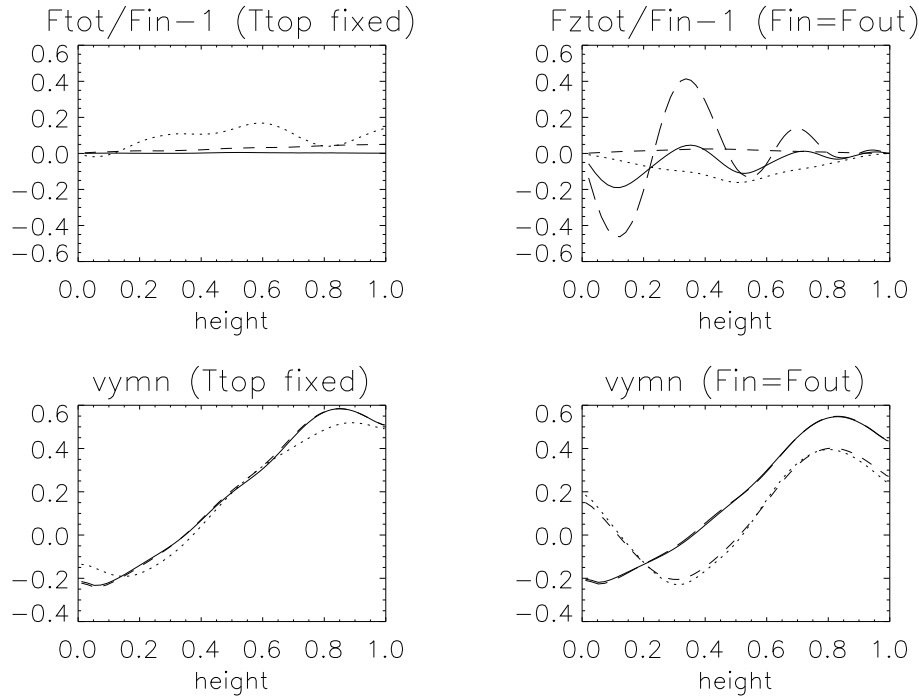


Figure 8. Profiles of the ‘averaged’ total flux (top panels) and zonal flow (lower panels) for the same case as Figure 7. Left panels are for the constant temperature upper boundary condition; Right panels are for the constant flux upper boundary condition. The averages are taken over different periods of time from start. The dotted, short dashed, solid, and long dashed curves are for the periods [98($\sim \tau_{th}/100$), 126], [270, 806], [1085($\sim \tau_{th}/10$), 1745], [1745, 2454], respectively. The mean flux of the constant flux case develops oscillations at later stages.

- Stix, M. 1987, in *The Internal Solar Angular Velocity*, ed. B. R. Durney & S. Sofia, (Dordrecht: Reidel), 329
- Sun, Z.-P. and Schubert, G. 1995, *Phys. Fluids*, 7, 2686
- Thompson, M. et al. 1996, *Science*, 272, 1300
- Tuominen, I. and Rudiger, G. 1989, *A&A*, 217, 217
- Wasiutynski, J. 1946, *Astrophys. Norvegica*, 4, 1
- Weiss, N.O. 1965, *Observatory*, 85, 37